Biomass Burning Emissions of Black Carbon over the Maritime Continent and ENSO Variability

BIYIN XIE,[a] YANG YANG,[a] HAILONG WANG,[b] PINYA WANG,[a] AND HONG LIAO[a]

[a] *Joint International Research Laboratory of Climate and Environment Change (ILCEC), Jiangsu Key Laboratory of Atmospheric Environment Monitoring and Pollution Control, Jiangsu Collaborative Innovation Center of Atmospheric Environment and Equipment Technology, School of Environmental Science and Engineering, Nanjing University of Information Science and Technology, Nanjing, Jiangsu, China*

[b] *Atmospheric Sciences and Global Change Division, Pacific Northwest National Laboratory, Richland, Washington*

(Manuscript received 21 July 2022, in final form 4 September 2023, accepted 8 September 2023)

ABSTRACT: Fire emissions from the Maritime Continent (MC) over the western tropical Pacific are strongly influenced by El Niño–Southern Oscillation (ENSO), posing various climate effects to the Earth system. In this study, we show that the historical biomass burning emissions of black carbon (BC_{bb}) aerosol in the dry season from the MC are strengthened in El Niño years due to the dry conditions. The eastern Pacific type of El Niño exerts a stronger modulation in BC_{bb} emissions over the MC region than the central Pacific type of El Niño. Based on simulations using the fully coupled Community Earth System Model (CESM), the impacts of increased BC_{bb} emissions on ENSO variability and frequency are also investigated in this study. With BC_{bb} emissions from the MC scaled up by a factor of 10, which enables the identification of climate response from the internal variability, the increased BC_{bb} heats the local atmosphere and changes land–sea thermal contrast, which suppresses the westward transport of the eastern Pacific surface water. It leads to an increase in sea surface temperature in the eastern tropical Pacific, which further enhances ENSO variability and increases the frequency of extreme El Niño and La Niña events. This study highlights the potential role of BC_{bb} emissions on extreme ENSO frequency, and this role may be increasingly important in the warming future with higher wildfire risks.

KEYWORDS: Maritime Continent; Atmospheric circulation; ENSO; Climate models; Aerosol radiative effect; Biomass burning

1. Introduction

El Niño–Southern Oscillation (ENSO) is the strongest interannual climate variation signal globally. It is characterized by anomalous sea surface temperature (SST) in the central-to-eastern tropical Pacific, oscillating irregularly between its warm (El Niño) and cold (La Niña) phases. These SST anomalies can alter atmospheric circulations and arouse teleconnection patterns (Bjerknes 1969), which exert pronounced global impacts on social stability and economic growth through modulating crop yields (Iizumi et al. 2014), drought and flood hazards (Jiménez-Muñoz et al. 2016; Ward et al. 2016), heat waves and cold surges (Thirumalai et al. 2017), tropical cyclones (Sobel and Maloney 2000), and ice melting in polar regions (Hu et al. 2016; Nicolas et al. 2017).

The Maritime Continent (MC) is the western boundary of the tropical Pacific under the ascending branch of the Walker circulation, which is susceptible to ENSO-related circulation changes. During the developing phase of El Niño, precipitation over the MC is suppressed, reducing the wet deposition of aerosols and promoting dry conditions favorable for fire burning (Chen et al. 2017; Wu et al. 2013). The severest fire years of the MC in the past few decades, such as 1991, 1997, and 2015, are all El Niño years (van Marle et al. 2017). Fire emissions during the major fire season of equatorial Asia were nearly tenfold higher during El Niño years than during La Niña years (Chen et al. 2017). In recent decades, biomass burning has become more frequent and widespread across the MC due to human activities, including land clearing, land-use change, poor peatland management, and burning of agriculture waste (Dennis et al. 2005; Marlier et al. 2015a; Lee et al. 2017). Large-scale and high-emission biomass burning activities occur every year in the dry season that usually peaks from August/September to October/November. Based on economic incentives and population growth in Southeast Asia, future land-use management will play an important role in determining fire activities across the region (Carlson et al. 2012; Marlier et al. 2015b). Furthermore, climate warming will generally increase the risk of fire and can also affect the fire injection and plume height (Szopa et al. 2021), which indicates that aerosol emissions from wildfire will increase in the future.

Changes in biomass burning aerosols over the MC could influence regional climate change. Biomass burning aerosols from fire emissions during El Niño events heat the middle and upper troposphere and cool the surface, thus increasing static stability near the surface. The increased stability, together with reduced specific humidity and weakened surface convergence, suppresses convection and precipitation, exacerbating drought in the source region of the MC (Tosca et al. 2010). During the extreme El Niño of 1997, carbonaceous aerosols from the Indonesian fires induced radiative forcings at the surface by about -10 W m^{-2} over most

Supplemental information related to this paper is available at the Journals Online website: https://doi.org/10.1175/JCLI-D-22-0553.s1.

Corresponding author: Yang Yang, yang.yang@nuist.edu.cn

DOI: 10.1175/JCLI-D-22-0553.1

of the tropical Indian Ocean and -150 W m^{-2} over the burning regions (Duncan et al. 2003).

Black carbon (BC) is an important component of aerosols emitted from incomplete combustion. Globally, open biomass burning accounts for about 15% of the total BC emissions. Long-term measurements in Indonesia (Rashid et al. 2014; Sattar et al. 2014) revealed that BC was elevated during the dry season because of the biomass burning emissions and relatively low rainfall. BC has diverse impacts on meteorology and climate by directly absorbing solar radiation within the atmospheric column, affecting cloud formation and lifetime, and reducing surface albedo through deposition on snow and ice (McFarquhar and Wang 2006; Ramanathan and Carmichael 2008; Kang et al. 2020). The influence of the heating effect of BC aerosols in the atmosphere depends on its vertical position. The BC-induced heating aloft increases stability below the BC layer and enhances vertical motion above the BC layer (Stocker et al. 2013). The warming effect of BC can be enhanced by coating its surface with organic carbon (OC), which leads to the "lensing effect" where photons are focused on the BC core (Lack and Cappa 2010). Compared to fossil fuel BC (BC_{ff}) emissions, biomass burning BC (BC_{bb}) is generally accompanied by higher emissions of OC, with a typical OC/BC ratio of 2 in urban traffic environments and a ratio of 5 or higher in regions with prevalent biomass burning emissions and smoldering dominance (Novakov et al. 2005). Also, BC_{bb} tends to be larger in size with thicker coatings compared to BC_{ff} in urban environments (Schwarz et al. 2008). Based on these characteristics, BC can exert significant climatic and dynamic impacts over the tropical Pacific and surrounding continents by changing atmospheric vertical motion, circulation, and convection. Increased BC emissions in the midlatitudes of the Northern Hemisphere and Arctic could increase the frequency of extreme ENSO events through altering meridional heat transport from equator to polar regions (Lou et al. 2019a). The direct radiative forcing of global BC can exert precipitation change patterns similar to those corresponding to ENSO activities (Wang 2007). BC from biomass burning and industrial emissions from the Indo-Gangetic Plain is also able to amplify the effect of ENSO on the Indian summer monsoon (Kim et al. 2016).

Previous studies have shown that the intensity and frequency of ENSO events might increase under climate warming (Stevenson 2012; Cai et al. 2014, 2015, 2018; Wang et al. 2018; B. Wang et al. 2019). Many studies have reported that aerosols and their precursor gases can affect ENSO properties, including its intensity, frequency, and duration. Fasullo et al. (2023) identified that 2019/20 Australian wildfires caused a significant increase in biomass aerosol burdens, altered cloud properties, and led to cooling in the tropical Pacific Ocean, ultimately contributing to the occurrence of strong La Niña events in 2020–22. Using simulations of global climate models, Yang et al. (2016a,b) found a positive sea salt emission–ENSO feedback, in which changes in sea salt emissions enhance the variability of ENSO. Xu and Yu (2019) investigated the ENSO-induced aerosol dipole over the international date line and the MC regions and proposed a positive feedback of aerosol dipole pattern to ENSO evolution. Several other studies found that stratospheric sulfate aerosols, formed from sulfur dioxide (SO_2) injected by tropical volcanic eruptions, influence the ENSO through changing the Earth radiation budget (Wang et al. 2018; Ward et al. 2021). How the increasing BC_{bb} from the MC potentially influences ENSO variability remains unexplored.

In this study, we show that the boreal winter mean Niño indices are positively correlated with the preceding September–November (SON) BC_{bb} emissions over the MC based on a long-term statistical analysis and analyze meteorological parameters leading to the increase of BC_{bb} emissions associated with El Niño. Then, the mechanism of the substantial increase in year-round BC_{bb} emissions from the MC regulating ENSO variability is identified based on long-term global aerosol–climate model simulations. The model, simulations, and observational datasets are described in section 2. The impacts of BC from the MC on ENSO variability and the potential mechanisms are analyzed in section 3. These results are summarized and discussed in section 4.

2. Methods

a. Data

The meteorological and aerosol emission datasets used in this study include the following:

1) For biomass burning emissions, we utilize the BB4CMIP dataset (available at https://esgf-node.llnl.gov/search/input4mips/; van Marle et al. 2017). BB4CMIP combines satellite-observed fire emissions with regional proxy datasets and modeled data to provide a global estimation of emissions of various aerosols and gases at a horizontal resolution of 0.25° × 0.25° and covers the period from 1750 to 2015 for the Coupled Model Intercomparison Project phase 6 (CMIP6). This dataset divides the world into 17 regions with different data sources. For the MC region in this study, the biomass burning emission data primarily originate from the equatorial Asia (EQAS) region within BB4CMIP. In the EQAS region, the emission data from 1997 to 2015 are based on the Global Fire Emissions Database version 4 with small fires (GFED4s). The emission data from 1950 to 1996 are based on visibility observations from the World Meteorological Organization (WMO) stations in the EQAS. However, the emission data from 1750 to 1949 are held constant at the lowest decadal average (van Marle et al. 2017). Therefore, in the EQAS region of BB4CMIP, the data from 1950 to 2015 are considered more reliable compared to the earlier period. In this study, for historical data analysis, we use BB4CMIP data from 1950 to 2015. For model input, we use data of 2006 that are regridded to 0.9° (latitude) × 1.25° (longitude) and divided into 13 levels.
2) For calculation of historical Niño indices, we utilize monthly sea surface temperature from the NOAA Extended Reconstructed SST V5 (ERSST v5; available at https://psl.noaa.gov/data/gridded/data.noaa.ersst.v5.html) with a horizontal resolution of 2° × 2° from 1950 to 2016.
3) For historical analysis of meteorological conditions for increasing BC_{bb} from the MC region during El Niño, we utilize

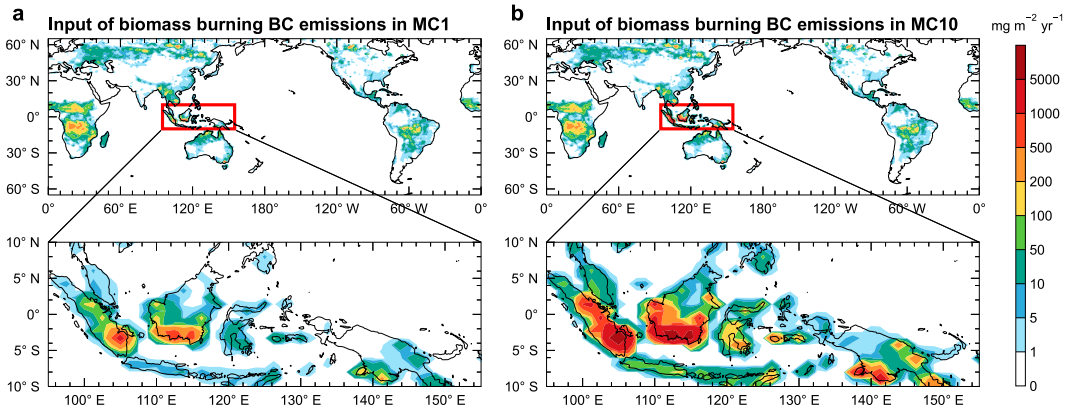

FIG. 1. Annual mean biomass burning black carbon emission rate (mg m^{-2} yr^{-1}) in (a) MC1 and (b) MC10 simulations. The red-outlined box marks the Maritime Continent (95°–155°E, 10°S–10°N). Biomass burning black carbon emission data are from the year 2006 of the BB4CMIP dataset.

monthly mean meteorological fields (i.e., sea level pressure, winds) from ERA5 reanalysis (available at https://cds.climate.copernicus.eu/; Hersbach et al. 2020) with a horizontal resolution of 0.25° × 0.25° from 1979 to 2015 and monthly mean precipitation from the Global Precipitation Climatology Project (GPCP; available at https://www.ncei.noaa.gov/data/global-precipitation-climatology-project-gpcp-monthly/access/; Adler et al. 2018) with a horizontal resolution of 2.5° × 2.5° from 1979 to 2015.

4) For anthropogenic emissions of model input, we use the Community Emissions Data System (CEDS; available at https://esgf-node.llnl.gov/search/input4mips/; Hoesly et al. 2018). Specifically, we use CEDS emissions of BC, OC, SO_2, and volatile organic compounds (VOCs) from various anthropogenic sectors in the year 2006. The CEDS emissions originally have a spatial resolution of 0.5° and are regridded to a resolution of 0.9° (latitude) × 1.25° (longitude) for our analysis and model simulation.

b. *Model configuration*

In this study, simulations are performed with the coupled global aerosol–climate model Community Earth System Model, version 1.2 (CESM1.2; Hurrell et al. 2013), which has been widely used to quantify aerosol–climate interactions (Yang et al. 2017, 2019, 2023; Lou et al. 2019a,b). The atmospheric component of CESM is the Community Atmosphere Model, version 5.3 (CAM5.3), configured with a 1.9° (latitude) × 2.5° (longitude) horizontal resolution and 30 vertical levels, in which mass and number concentrations of aerosols—including sulfate (SO_4^{2-}), BC, primary organic matter (POM), secondary organic aerosol (SOA), mineral dust, and sea salt—are represented using the four-mode (i.e., Aitken, accumulation, coarse, and primary carbon modes) Modal Aerosol Module (MAM4; Liu et al. 2016). MAM4 is chosen for its aging processes of primary carbonaceous aerosols that can well represent the BC aerosol life cycle. The CAM5.3 model includes aerosol–radiation interaction in shortwave and longwave bands as well as aerosol–cloud interactions for stratiform clouds (Liu et al. 2012). In our model simulations, to estimate the direct radiative forcing (DRF) of BC, atmospheric radiation calculation is performed twice with BC included and excluded, respectively, in the estimate of bulk aerosol properties for the radiative transfer model. The ocean component is the Parallel Ocean Program, version 2 (POP2), configured with the nominal grid gx1v6 (horizontal resolution of approximately 1°) and with 60 vertical levels.

To assess the impact of BC_{bb} on ENSO variability, two experiments are conducted, namely, MC1 and MC10, both of which are initialized with the same atmosphere and ocean conditions at present-day levels. In the MC1 experiment, solar radiation, greenhouse gases concentration, and aerosol and precursor emissions are all fixed at year 2006 level with monthly variations, while in the MC10 case, BC_{bb} emissions of each month over the MC (95°–155°E, 10°S–10°N) are scaled up by a factor of 10 and other regions are kept the same as MC1. The reason for choosing emissions in the year 2006 as the baseline is that biomass burning aerosols over the MC are significantly affected by a moderate El Niño in 2006 (Chandra et al. 2009). Therefore, the emissions in 2006 are relatively higher than normal but not too extreme compared to strong El Niño years (Fig. S1 in the online supplemental material), which helps to distinguish the climate response signals from the internal variability. The input of BC_{bb} emissions in MC1 and MC10 is shown in Fig. 1. The large increase (i.e., the factor of 10) is used in MC10 so that climate response signals are stronger than internal variability in the climate model, which has been widely used in previous aerosol perturbation experiments (e.g., Lou et al. 2019a,b; Sand et al. 2013, 2015; Stjern et al. 2017; Yang et al. 2019). MC1 and MC10 cases are initialized with the same present-day default initial condition. For each experiment, one 135-yr simulation is performed with the last 100 years used for model analysis and the first 35 years treated as model spinup time.

c. *Model evaluation*

We compare the global patterns and seasonal variations over the MC between reanalyzed/satellite data and simulated

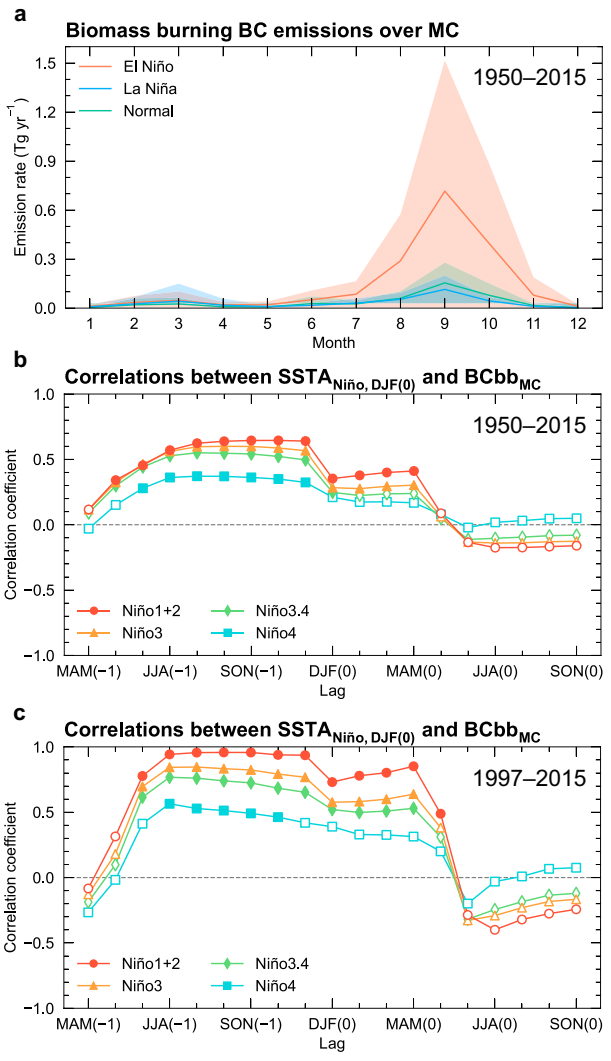

FIG. 2. Historical relationship between biomass burning black carbon emissions over the Maritime Continent and El Niño–Southern Oscillation. (a) Seasonal variation of biomass burning black carbon emission rate (Tg yr^{-1}) over the Maritime Continent during 1950–2015. The shading indicates one standard deviation. El Niño years are 1951, 1953, 1957, 1963, 1965, 1968, 1969, 1972, 1976, 1977, 1982, 1986, 1987, 1991, 1994, 1997, 2002, 2004, 2006, 2009, and 2015. La Niña years are 1950, 1954, 1955, 1956, 1964, 1970, 1971, 1973, 1974, 1975, 1984, 1988, 1995, 1998, 1999, 2000, 2005, 2007, 2008, 2010, and 2011. (b) Lead–lag correlations between the December–February mean Niño indices and the biomass burning black carbon emission rate over the Maritime Continent during 1950–2015. The "−1" and "0" on the *x* axis labels represent the preceding and following year, respectively, and the statistically significant correlations (at the 95% level) are marked by solid markers. (c) As in (b), but the data are during 1997–2015. Biomass burning black carbon emission data are from the BB4CMIP dataset. Niño indices are calculated from ERSST v5.

results. The simulated absorption aerosol optical depth of BC (AAODBC) from the MC1 case is contrasted with the reanalysis data of MERRA2 (M2TMNXAER) (Fig. S2), revealing an underestimation of AAODBC over the MC region by the model. This may be attributed to the bias in BC aerosol simulation related to many factors including emissions and wet scavenging, as well as the bias in satellite retrievals related to abundance of clouds over the MC region. Remarkably, the simulated total cloud fraction demonstrated a strong correspondence with the MODIS satellite data (Fig. S3). Additionally, the simulated precipitation rate (Fig. S4) closely resembled the magnitude observed in the GPCP reanalysis data. However, it is noteworthy that CESM1.2, like many climate models, exhibited a tendency to simulate a double intertropical convergence zone (ITCZ) rather than the conventional single band. Also, the 2° version of CESM1.2 tends to simulate more extreme ENSO events than those in the real world (Lou et al. 2019a).

d. ENSO indices and statistical methods

The intensity of ENSO condition is usually characterized by monthly Niño indices, including the Niño-1 + 2, Niño-3, Niño-3.4, and Niño-4 indices, which are defined as the regionally averaged SST anomalies over the Niño-1 + 2 region (90°–80°W, 10°–0°S), Niño-3 region (150°–90°W, 5°S–5°N), Niño-3.4 region (170°–120°W, 5°S–5°N), and Niño-4 region (160°E–150°W, 5°S–5°N), respectively. The Niño indices are calculated from ERSST v5 and used for the selection of historical El Niño years and the correlation analysis.

An El Niño (La Niña) event is usually identified based on the Niño-3.4 index. In the section of the impact of El Niño on BC_{bb} emissions from the MC, El Niño years during 1950–2015 are identified using the Niño-3.4 index according to the method used by the Climate Prediction Center (CPC) of NOAA. First, the interannual linear trend from 1950 to 2016 is removed from the monthly averaged SST in the Niño-3.4 region. Then, the anomalies of Niño-3.4 SST with the seasonal variations removed are calculated. A consecutive 5-month moving average exceeding 0.5°C is considered as an El Niño event. The selected El Niño years during 1950–2015 are 1951, 1953, 1957, 1963, 1965, 1968, 1969, 1972, 1976, 1977, 1982, 1986, 1987, 1991, 1994, 1997, 2002, 2004, 2006, 2009, and 2015. In the section of the impact of BC_{bb} emissions from the MC on ENSO, we use the standard of Santoso et al. (2017) to identify extreme El Niño/La Niña events in the model results. If the Niño-3.4 SST anomalies of November–January (NDJ) [or December–February (DJF)] exceed one standard deviation of Niño-3.4 SST anomalies of NDJ (or DJF) in MC1, it is classified as an extreme El Niño or La Niña event. The standard deviation of NDJ (DJF) in MC1 is 2.1°C (2.0°C).

The statistical significance of changes in the occurrence frequency of ENSO conditions between the two simulations is tested in two steps. We first construct a Kolmogorov–Smirnov test to examine whether the frequency distribution of the Niño-3.4 index from MC10 differs from that of MC1. Next, SST data obtained from a 1400-yr CESM preindustrial simulation are used as a baseline to examine whether the frequency within a specific interval has changed in MC10 compared to MC1. Specifically, we construct a probability distribution function (PDF) for each 1-K interval of the monthly Niño-3.4 index using 1000 random samples of consecutive 1200-month results from the 1400-yr CESM control simulation with a Monte Carlo method. Within each 1-K interval, if the difference between MC1 and

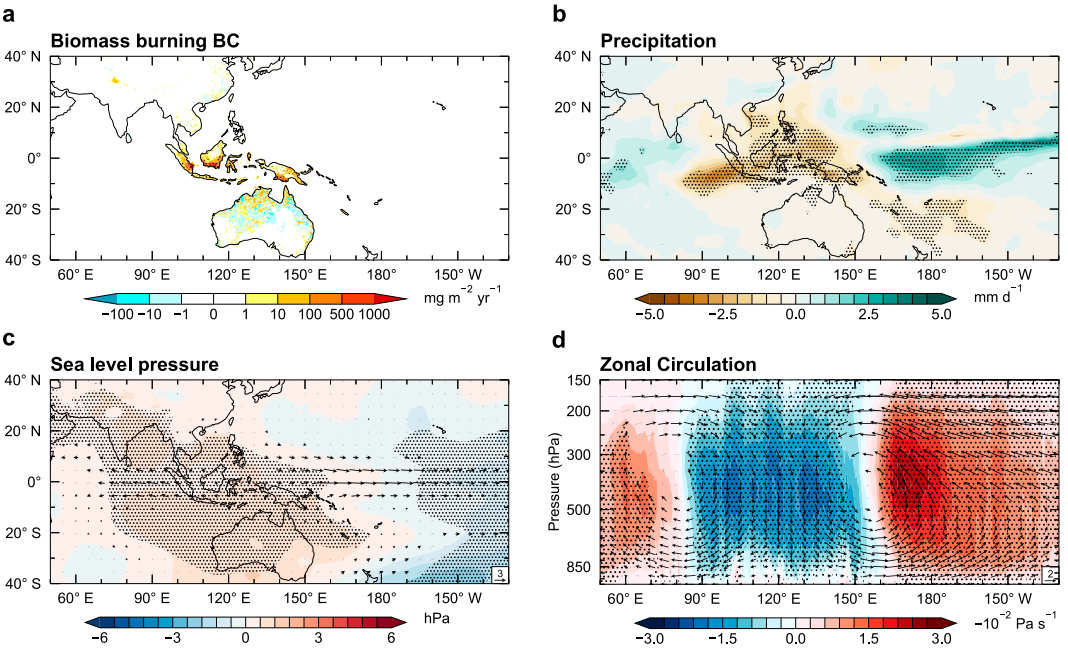

FIG. 3. Anomalies in boreal fall season preceding El Niño events compared to the climatology in (a) biomass burning black carbon emission rate (mg m^{-2} yr^{-1}), (b) precipitation (mm day^{-1}), (c) sea level pressure (hPa) and 10-m winds (m s^{-1}), and (d) zonal circulation (reference vector) and pressure velocity (contours; -10^{-2} Pa s^{-1}). Biomass burning black carbon emission data are from the BB4CMIP dataset. Meteorological parameters are from GPCP and ERA5 reanalysis. The dotted areas indicate statistical significance more than 95% confidence level from a two-tailed Student's *t* test. The black vectors indicate that the statistical significance of latitudinal winds or meridional (vertical) winds is more than 95% confidence level from a two-tailed Student's *t* test, while the gray vectors indicate the insignificant winds. The climatology is based on 1950–2015. El Niño years are 1951, 1953, 1957, 1963, 1965, 1968, 1969, 1972, 1976, 1977, 1982, 1986, 1987, 1991, 1994, 1997, 2002, 2004, 2006, 2009, and 2015, which are selected by the method of NOAA CPC.

MC10 is greater than the 95th percentile or less than the 5th percentile of the PDF, the change in the Niño-3.4 index distribution of the interval is considered significant. However, we note that the statistical analysis based on a preindustrial simulation could overestimate the significance of the ENSO differences between MC1 and MC10, since that the preindustrial simulation has a weaker SST variability than MC1/MC10 (Table S1). Also, the preindustrial simulation is performed using CESM version 1.1 (see Text S1 in the online supplemental material), which is the prior version of CESM1.2 for MC1 and MC10 simulations. However, the two model versions share very similar ENSO statistics and should not affect the results in this study.

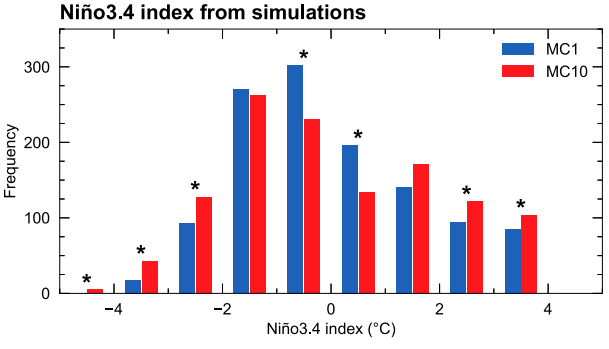

FIG. 4. Frequency distribution of the monthly Niño-3.4 index (°C) of 1200 months from MC1 (blue bars) and MC10 (red bars). Bars with asterisks indicate statistically significant changes with respect to the upper and lower 5th percentiles of a probability distribution function for each Niño-3.4 index bin derived from a 1400-yr CESM preindustrial simulation.

3. Results

a. *Impact of ENSO on fire emissions of BC over the Maritime Continent*

From the perspective of the annual cycle, the BC_{bb} emission rate over the MC peaks in the late boreal summer and boreal fall seasons and the emissions increase during the El Niño years (Fig. 2a). ENSO events usually reach their peak intensity during boreal winter. To examine whether BC_{bb} emissions over the MC change with the ENSO phase and intensity, the lead–lag correlation coefficients between the DJF mean Niño indices and the BC_{bb} emission rate over the MC in the preceding and following seasons during 1950–2015 are calculated and shown in Fig. 2b. The BC_{bb} emission rate over the MC in the fall season preceding the boreal winter of the mature phase of ENSO events is positively correlated with Niño indices, with correlation

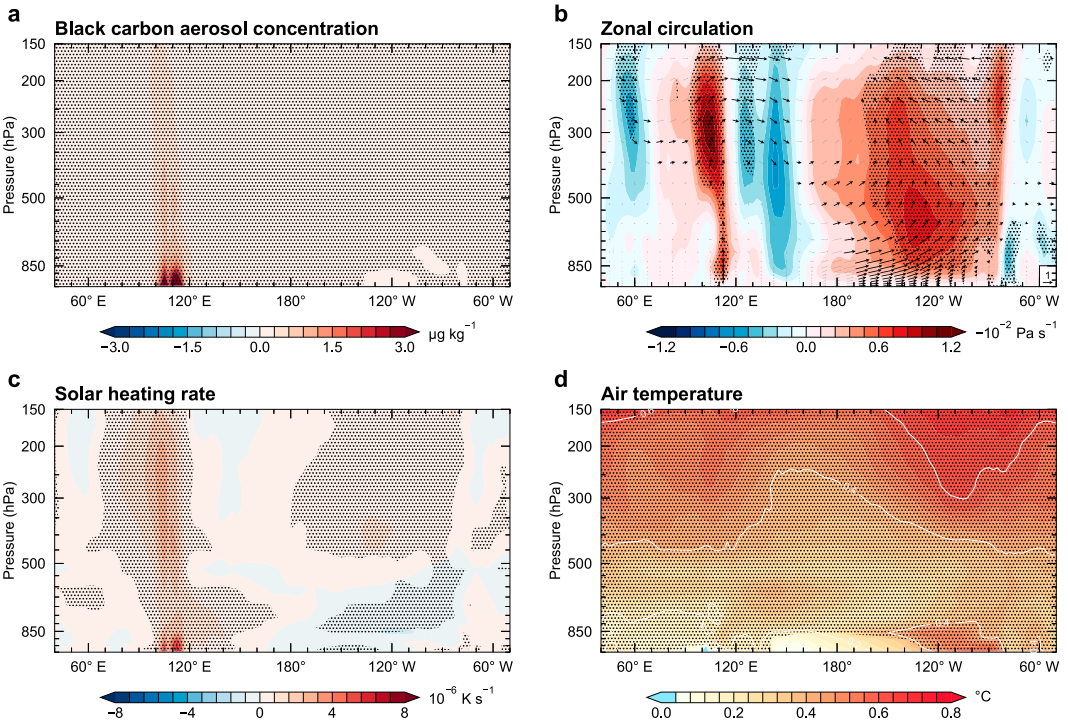

FIG. 5. Pressure–longitude cross sections averaged over 3°S–0° of differences between the MC1 and MC10 cases for (a) black carbon aerosol concentration (μg kg^{-1}), (b) zonal circulation (reference vector) and vertical velocity (contours; -10^{-2} Pa s^{-1}), (c) shortwave heating rate (10^{-6} K s^{-1}), and (d) air temperature (°C). In (b), the red shading indicates rising motion as the contour scale is negative. The differences are calculated from simulated data by ($V_{\text{annual,MC10}} - V_{\text{annual,MC1}}$). $V_{\text{annual,MC1}}$ is the annual mean of 100 years in MC1 case for each parameter. The same holds for $V_{\text{annual,MC10}}$ but in the MC10 case. The dotted areas indicate statistical significance more than 95% confidence level from a two-tailed Student's t test. The black vectors indicate that the statistical significance of latitudinal winds or vertical winds is more than 95% confidence level from a two-tailed Student's t test, while the gray vectors indicate the insignificant winds.

coefficients of 0.6–0.9 for Niño-1 + 2, Niño-3, and Niño-3.4 indices, and is statistically significant at 95% confidence level. If the lead–lag correlation is based on 1997–2015 when biomass burning data are all derived from satellite observations, the correlations will be higher with the correlation coefficient between the Niño-1 + 2 index and BC_{bb} emission rate exceeding 0.95 (Fig. 2c). It suggests that the biomass burning emissions of BC are enhanced during El Niño events, especially in the preceding fall season. The Niño-1 + 2 index has the highest correlation with the BC_{bb} emission rate, while the Niño-4 index has the lowest correlation coefficient, indicating that the eastern Pacific type of El Niño exerts a stronger modulation in BC_{bb} emissions over the MC region than the central Pacific type of El Niño.

From the perspective of the annual cycle of precipitation climatology, boreal fall is the dry season in the MC region with relatively little precipitation (Zhang et al. 2016). In general, the MC is under the ascending branch of the Walker circulation. However, during the developing phase of El Niño, the updraft vertical motion is suppressed (Fig. 3d), which coincides with the increased sea level pressure over the region spanning from the eastern Indian Ocean to the west Pacific warm pool (Fig. 3c). A weakened convection due to the suppressed updraft decreases the precipitation over the MC and the eastern Indian Ocean (Fig. 3b). The dry condition over the MC is favorable for fire occurrence. The increased fires also release more heat, which is conductive to temperature increase and further worsens the dry conditions. The intensified fire activities increase BC emissions into the air (Fig. 3a), which are likely to reside in the air for a longer time under dry conditions (Wu et al. 2013).

b. *Biomass burning BC from the Maritime Continent enhances ENSO variability*

The analysis above points out that BC emissions from biomass burning over the MC increase during the preceding boreal fall seasons of El Niño events from the perspective of the annual cycle. The strongly increased BC_{bb} can also impact ENSO statistics via its radiative effects. The standard deviation of the monthly Niño-3.4 index after removing the annual cycle simulated in CESM increases from 1.69°C in MC1 to 1.92°C in MC10. It implies that substantial increases in BC emissions from biomass burning over the MC could enhance ENSO variability.

Figure 4 shows histograms of the monthly Niño-3.4 index obtained from the MC1 and MC10 simulations. The frequency

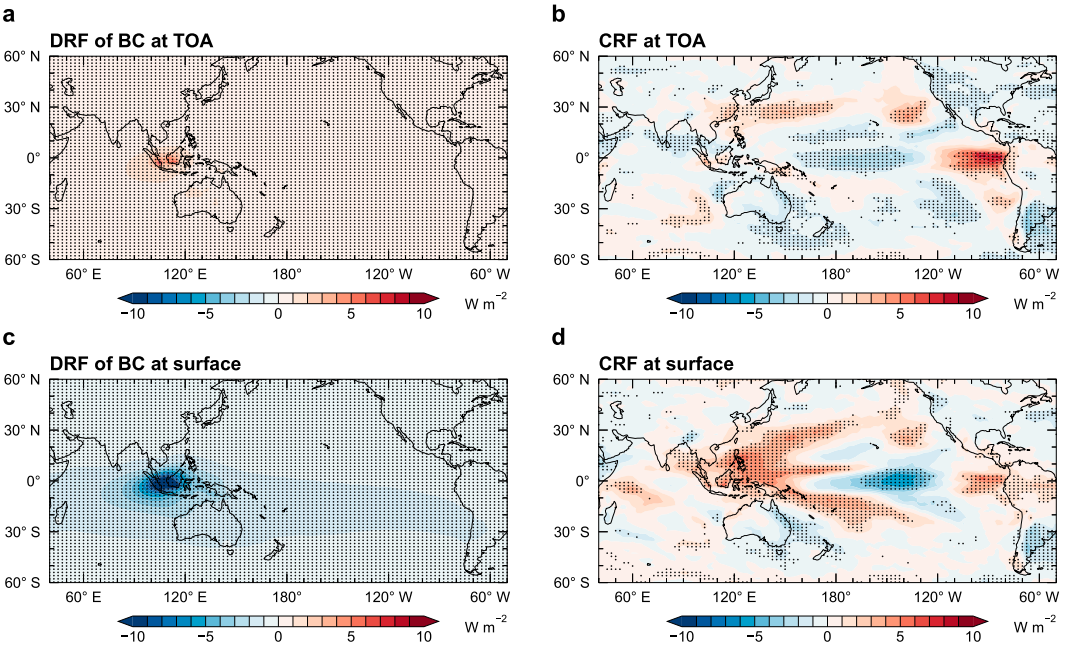

FIG. 6. Differences in radiative effects (W m^{-2}) between the MC1 and MC10 cases, including direct radiative forcing (DRF) caused by black carbon at (a) the top of atmosphere and (c) the surface as well as net cloud radiative forcing (CRF) at (b) the top of atmosphere and (d) the surface. The differences are calculated from simulated data by ($V_{annual,MC10} - V_{annual,MC1}$). $V_{annual,MC1}$ is the annual mean of 100 years in the MC1 case for each parameter. The same holds for $V_{annual,MC10}$ but in the MC10 case. The dotted areas indicate statistical significance more than 95% confidence level from a two-tailed Student's *t* test.

distribution of the Niño-3.4 index in MC10 is different from that in MC1 based on the Kolmogorov–Smirnov test ($p < 0.01$). The frequencies at the positive and negative tails of the monthly Niño-3.4 index significantly increase in MC10, indicating that the increase in BC_{bb} over the MC may enhance the ENSO variability and increase the frequency of extreme ENSO events. If the ENSO years are identified based on the NDJ or DJF mean Niño-3.4 index, the frequencies of extreme El Niño (La Niña) events change from 23 (16) per 100 years in MC1 to 25 (19) per 100 years in MC10.

c. *Potential mechanisms of BC impacts on ENSO variability*

Potential mechanisms of how BC_{bb} affects the ENSO variability are examined here. We investigate the pressure–longitude cross sections averaged over 3°S–0° of the difference in BC concentration, zonal circulation, shortwave heating rate, and air temperature in Fig. 5. The latitude band of 3°S–0° is chosen because it can better show the BC plume from the high emission area over the MC (Fig. 1). The tenfold increase in BC_{bb} emissions in the MC leads to a strong increase in BC concentrations between 100° and 120°E near the equator (Fig. 5a). The maximum increase locates below 850 hPa and it extends to the upper troposphere. As the most important absorbing aerosol, BC heats the atmosphere through absorbing solar radiation. With the increase in BC aerosol concentration, the shortwave atmospheric heating rate is enhanced over the MC (Fig. 5c). While the BC concentration primarily rises in the lower troposphere, the anomalous shortwave heating exerts a strong influence throughout the entire atmospheric column, owing to the efficient solar absorption of BC at higher altitudes. Additionally, the reduction in cloud coverage associated with a dearth of precipitation also contributes to the shortwave heating.

Over the MC (95°–155°E, 10°S–10°N), the tenfold increase in BC_{bb} emissions induces a DRF of 1.3 W m^{-2} at the top of atmosphere (TOA) and of −4.4 W m^{-2} at the surface (Figs. 6a,c), showing a strong solar absorption of 5.7 W m^{-2} in the atmosphere. The anomalous heating in the atmospheric column induces a strong ascending motion above the BC layer between 105° and 115°E (Fig. 5b). The enhanced updraft is accompanied by an anomalous subsidence over 120°–160°E of the tropical Pacific (Fig. 5b), which coincides with the increasing sea level pressure over the western Pacific (Fig. 7a). In the lower troposphere over the western Pacific, the subsidence is expected to diverge. One anomalous horizontal branch moves toward east over the central tropical Pacific (Figs. 5b and 7b). Under normal circumstances, the easterly trade winds move the sea surface water from the eastern tropical Pacific to the west. Meanwhile, the upwelling of cold water from the deep sea cools the sea surface over the eastern tropical Pacific, resulting in lower SST in the eastern tropical Pacific than in the western Pacific. However, in the MC10 case, the westerly wind anomaly weakens the easterly trade winds, causing a reduced transport of sea surface water from east to west. As a result, the east–west SST gradient is weakened by the substantial increase in BC_{bb} emissions over the MC, leading to the anomalous warming over the eastern

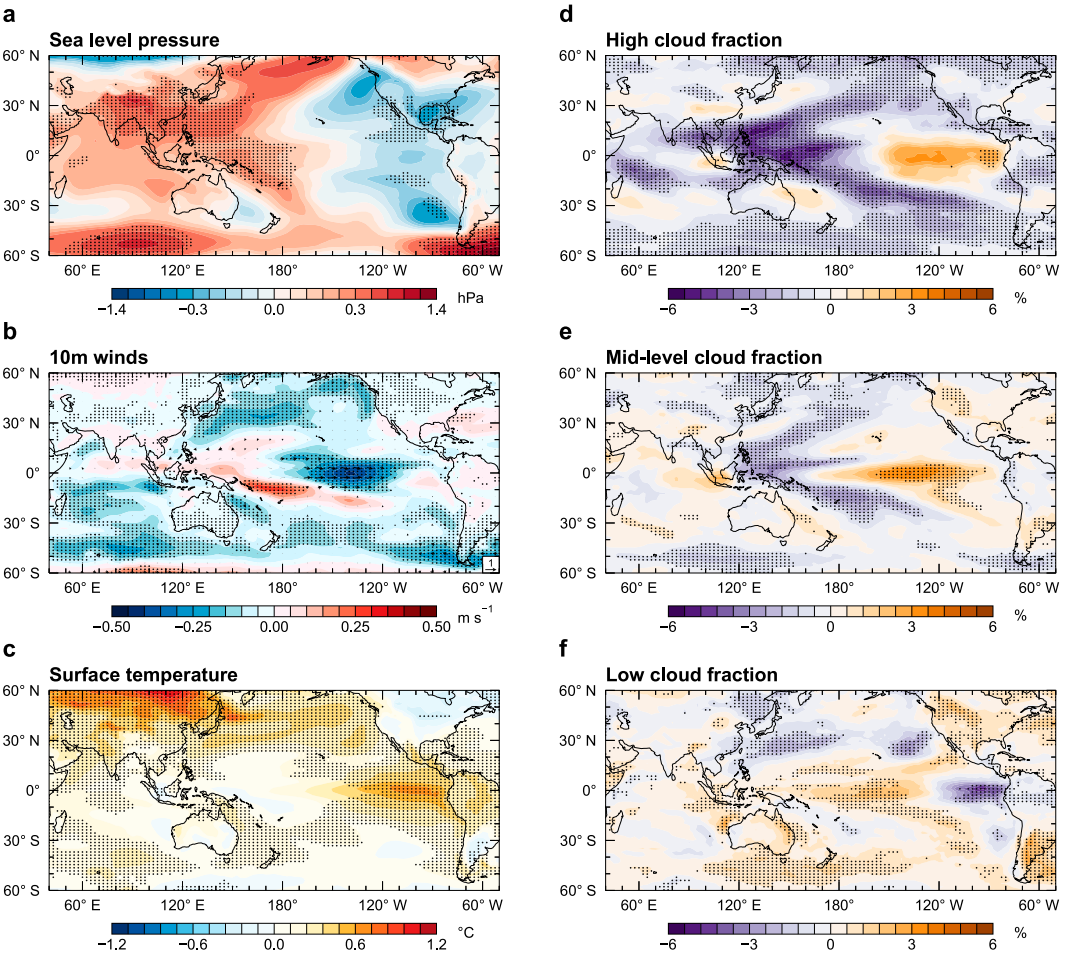

FIG. 7. Differences between MC1 and MC10 cases in (a) sea level pressure (hPa), (b) 10-m wind vectors and speeds ($m\ s^{-1}$), (c) surface temperature (°C), (d) high cloud fraction (%), (e) midlevel cloud fraction (%), and (f) low cloud fraction (%). The differences are calculated from simulated data by ($V_{annual,MC10} - V_{annual,MC1}$). $V_{annual,MC1}$ is the annual mean of 100 years in the MC1 case for each parameter. The same holds for $V_{annual,MC10}$ but in the MC10 case. The dotted areas indicate statistical significance more than 95% confidence level from a two-tailed Student's t test. The black vectors indicate that the statistical significance of latitudinal winds or meridional winds is more than 95% confidence level from a two-tailed Student's t test, while the gray vectors indicate the insignificant winds.

tropical Pacific (Figs. 5d and 7c). The anomalous warming of sea surface water causes the anomalous upward motion of the atmosphere around 130°W (Fig. 5b), leading to a decrease in low cloud fraction and an increase in high cloud fraction (Figs. 7d,f). In the atmosphere, low clouds mainly scatter solar radiation and pose net cooling effect to the Earth system, while high clouds consist chiefly of ice crystals, which can absorb the longwave radiation from the surface and heat the earth. The change in the vertical profile of cloud amount leads to a positive cloud radiative forcing (CRF) over the eastern tropical Pacific (Figs. 6b,d), which is also conductive to sea surface warming (Fig. 7c). Over the central Pacific, the increased low clouds and midlevel clouds (Figs. 7e,f) induce a negative CRF over this region (Figs. 6b,d).

Due to the effects of weakened easterly trade winds and positive CRF, the SST over the eastern tropical Pacific in the MC10 case increases significantly relative to the MC1 case, which further enhances ENSO variability and increases the frequency of extreme ENSO events. Y. Wang et al. (2019) found that a uniform sea surface warming could increase ENSO amplitudes and the frequency of ENSO events. Previous studies also showed that faster warming in the eastern tropical Pacific than in other regions due to westerly wind anomalies in the equatorial Pacific under global warming (Xie et al. 2010) could promote an increase in the frequency of extreme El Niño events (Cai et al. 2014, 2022). It is consistent with this study that the warming over the eastern tropical Pacific due to the tenfold increase in BC_{bb} emissions increases the frequency of extreme El Niño events. Some studies have shown that a La Niña–like change occurs in the mean state of SST across the equatorial Pacific due to the damping effect of upwelling seawater in the eastern equatorial Pacific on the increase of SST (Latif and Keenlyside 2009; Lian et al. 2018). Cai et al. (2015) argued that a faster warming rate of the MC

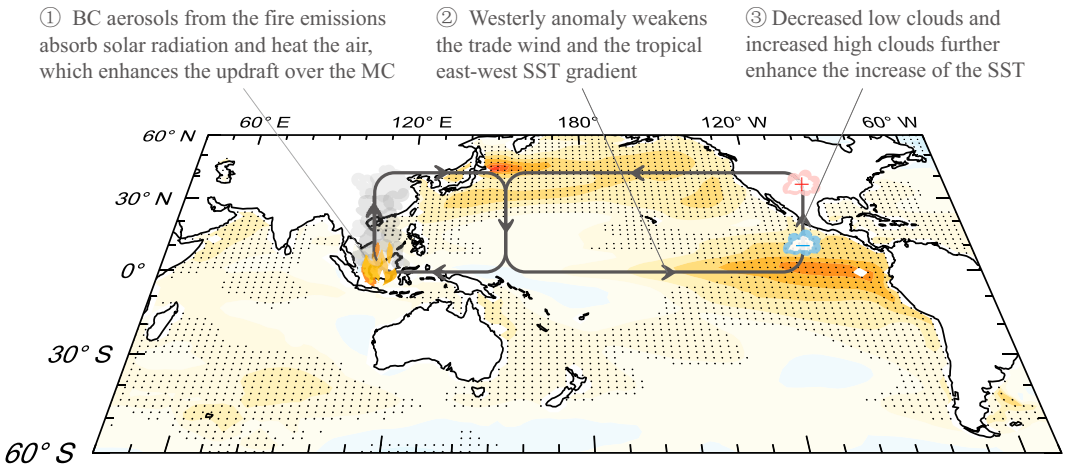

FIG. 8. Mechanism of the impacts of biomass burning black carbon aerosol emissions from the Maritime Continent on El Niño–Southern Oscillation. Color shading represents the difference in sea surface temperature between the MC1 and MC10 cases. Arrows indicate the difference in atmospheric circulation between the MC1 and MC10 cases. The schematic highlights the tropical Pacific mean state changes in response to enhanced black carbon emissions over the Maritime Continent. The change in El Niño–Southern Oscillation statistics can then follow the mean state changes but is likely model dependent.

than the central equatorial Pacific enhanced upper ocean vertical temperature gradients in the central equatorial Pacific, and the increased frequency of extreme El Niño events is conducive to the development of extreme La Niña events. These support our finding that the frequency of extreme La Niña events is enhanced due to the tenfold increase in BC_{bb}.

4. Conclusions and discussion

In this study, we investigate the meteorological parameters leading to the increase of BC_{bb} emissions over the MC associated with El Niño and then examine the impact of substantial increases in BC_{bb} emissions on the ENSO variability and the frequency of extreme ENSO events using CESM model sensitivity experiments. The BC_{bb} emissions over the MC in the fall season preceding the boreal winter of the mature phase of ENSO events are positively correlated with Niño indices. El Niño can increase the biomass burning emissions over the MC by enhancing the dry conditions. We also show that the eastern-Pacific type of El Niño exerts a stronger modulation in BC_{bb} emissions over the MC region than the central-Pacific type of El Niño.

A tenfold increase of BC_{bb} emissions over the MC substantially warms the atmosphere and enhances the ascending air motion above the BC layer over the MC, leading to changes in the atmospheric circulation over the western Pacific. The changed atmospheric circulation further weakens the near-surface easterly trade winds over the central-to-eastern tropical Pacific and weakens the east–west SST gradient, which reduces the upwelling of mean cold subsurface water and leads to an increase in SST over the eastern tropical Pacific. Meanwhile, the low cloud fraction decreases and the high cloud fraction increases over the eastern tropical Pacific, which further enhances the increase in SST. When the mean SST increases over the eastern tropical Pacific, ENSO variability is enhanced and the frequency of extreme El Niño and La Niña events is increased due to the tenfold increase of BC_{bb} emissions over the MC, as simulated in the CESM experiments. It highlights that there might be more extreme ENSO events if there were more BC_{bb} emissions from the MC in a warmer future. The mechanism of the impacts of BC_{bb} aerosol emissions from the MC on ENSO is illustrated in the schematic in Fig. 8.

There are some limitations and uncertainties in the study. Concerning the experimental design for exploring the interaction between BC_{bb} and ENSO, two key factors need to be considered. First, current models lack the capability of online calculation of BC_{bb} emissions. Second, the oceanic responses are much slower than the atmosphere. On the background of these factors, the direct response of BC emissions over the MC region to individual El Niño events and the influence of the large increase in BC emissions on ENSO statistical probability due to mean state changes are separately analyzed in this study with different time scales. In the real world, the loop linking the increased BC emissions during an El Niño event back to another ENSO event could be hidden by the internal variability. Besides, any change in extreme ENSO events in the real world is difficult to attribute to the changing aerosols due to their weak forcing compared to natural variability. To address these challenges, the annual BC_{bb} emissions from the MC region are amplified by a factor of 10 in the CESM simulation (MC10) for investigating the BC impact on ENSO. It allows the signal of climate response to BC to be stronger than the internal variability of the climate model, and such a large perturbation was also adopted in previous studies (e.g., Lou et al. 2019a,b; Sand et al. 2013, 2015; Stjern et al. 2017; Yang et al. 2019). However, in the real world, it is unrealistic that BC_{bb} emissions over the MC associated with El Niño alone can reach 10 times of that in 2006, which is a relatively high emission year affected by a moderate El Niño.

When conducting model simulations in this study, the atmosphere component focuses on the troposphere with 30 vertical levels from the surface to about 3.6 hPa. However, the biomass burning aerosol can also induce deep convection due to their release of sensible heat and affect stratospheric climate (Trentmann et al. 2006; Chavan et al. 2021). Whether BC emissions from the MC can affect stratospheric climate and feedback on ENSO requires further studies using a high-top atmospheric model.

The response of ENSO variability to external climate forcing in model simulations remains a controversial topic, as ENSO is largely influenced by a delicate balance of multiple amplification and damping feedbacks. As indicated in Lou et al. (2019a), the 2° version of CESM1.2 simulates more extreme ENSO events than observations. We use the 2° atmosphere configuration because the ENSO variability requires long-term simulations and the 2° atmosphere configuration is much more efficient than the 1° configuration. Also, the model resolution and version are consistent with our previous study (Lou et al. 2019a), although it may not be the most accurate model version in simulating ENSO statistics. Some modeling studies show weakened ENSO variability under a warming climate (Kohyama et al. 2018), while CESM results showed the opposite (Y. Wang et al. 2019). Therefore, we cannot rule out the model dependence of these simulation results. Also, the 100-yr results may not be long enough to fully capture the ENSO statistics. These deserve further exploration with multimodels, large ensembles, and long-term simulations in future studies.

In this study, we focused on BC emissions from the MC region, but we also note that ENSO modulates fire across the tropics with some influences being potentially constructive and other aspects being destructive, which also requires future investigation.

Acknowledgments. This research was supported by the National Natural Science Foundation of China (Grant 41975159), the Jiangsu Science Fund for Distinguished Young Scholars (Grant BK20211541), and the Jiangsu Science Fund for Carbon Neutrality (Grant BK20220031). H. W. acknowledges the support by the U.S. Department of Energy (DOE), Office of Science, Office of Biological and Environmental Research (BER), as part of the Earth and Environmental System Modeling program. The Pacific Northwest National Laboratory (PNNL) is operated for DOE by Battelle Memorial Institute under Contract DE-AC05-76RLO1830.

Data availability statement. The emission data (i.e., BB4CMIP, CEDS) are available from https://esgf-node.llnl.gov/search/input4mips/. ERSST v5 sea surface temperature data are available from https://psl.noaa.gov/data/gridded/data.noaa.ersst.v5.html. ERA5 reanalysis data are available from https://cds.climate.copernicus.eu/. GPCP precipitation data are available from https://www.ncei.noaa.gov/data/global-precipitation-climatology-project-gpcp-monthly/access/. SST data from a 1400-yr CESM preindustrial control simulation are available from https://www.earthsystemgrid.org/dataset/ucar.cgd.ccsm4.b.e11.B1850C5CN.f19_g16.008.atm.proc.monthly_ave.TS.html. The processed modeling data are available at https://doi.org/10.5281/zenodo.7312877.

REFERENCES

Adler, R. F., and Coauthors, 2018: The Global Precipitation Climatology Project (GPCP) monthly analysis (new version 2.3) and a review of 2017 global precipitation. *Atmosphere*, **9**, 138, https://doi.org/10.3390/atmos9040138.

Bjerknes, J., 1969: Atmospheric teleconnections from the equatorial Pacific. *Mon. Wea. Rev.*, **97**, 163–172, https://doi.org/10.1175/1520-0493(1969)097<0163:ATFTEP>2.3.CO;2.

Cai, W., and Coauthors, 2014: Increasing frequency of extreme El Niño events due to greenhouse warming. *Nat. Climate Change*, **4**, 111–116, https://doi.org/10.1038/nclimate2100.

——, and Coauthors, 2015: Increased frequency of extreme La Niña events under greenhouse warming. *Nat. Climate Change*, **5**, 132–137, https://doi.org/10.1038/nclimate2492.

——, and Coauthors, 2018: Increased variability of eastern Pacific El Niño under greenhouse warming. *Nature*, **564**, 201–206, https://doi.org/10.1038/s41586-018-0776-9.

——, B. Ng, G. Wang, A. Santoso, L. Wu, and K. Yang, 2022: Increased ENSO sea surface temperature variability under four IPCC emission scenarios. *Nat. Climate Change*, **12**, 228–231, https://doi.org/10.1038/s41558-022-01282-z.

Carlson, K. M., and Coauthors, 2012: Committed carbon emissions, deforestation, and community land conversion from oil palm plantation expansion in West Kalimantan, Indonesia. *Proc. Natl. Acad. Sci. USA*, **109**, 7559–7564, https://doi.org/10.1073/pnas.1200452109.

Chandra, S., J. R. Ziemke, B. N. Duncan, T. L. Diehl, N. J. Livesey, and L. Froidevaux, 2009: Effects of the 2006 El Niño on tropospheric ozone and carbon monoxide: Implications for dynamics and biomass burning. *Atmos. Chem. Phys.*, **9**, 4239–4249, https://doi.org/10.5194/acp-9-4239-2009.

Chavan, P., S. Fadnavis, T. Chakroborty, C. E. Sioris, S. Griessbach, and R. Müller, 2021: The outflow of Asian biomass burning carbonaceous aerosol into the upper troposphere and lower stratosphere in spring: Radiative effects seen in a global model. *Atmos. Chem. Phys.*, **21**, 14 371–14 384, https://doi.org/10.5194/acp-21-14371-2021.

Chen, Y., D. C. Morton, N. Andela, G. R. van der Werf, L. Giglio, and J. T. Randerson, 2017: A pan-tropical cascade of fire driven by El Niño/Southern Oscillation. *Nat. Climate Change*, **7**, 906–911, https://doi.org/10.1038/s41558-017-0014-8.

Dennis, R. A., and Coauthors, 2005: Fire, people and pixels: Linking social science and remote sensing to understand underlying causes and impacts of fires in Indonesia. *Hum. Ecol.*, **33**, 465–504, https://doi.org/10.1007/s10745-005-5156-z.

Duncan, B. N., I. Bey, M. Chin, L. J. Mickley, T. D. Fairlie, R. V. Martin, and H. Matsueda, 2003: Indonesian wildfires of 1997: Impact on tropospheric chemistry. *J. Geophys. Res.*, **108**, 4458, https://doi.org/10.1029/2002JD003195.

Fasullo, J. T., N. Rosenbloom, and R. Buchholz, 2023: A multiyear tropical Pacific cooling response to recent Australian wildfires in CESM2. *Sci. Adv.*, **9**, eadg1213, https://doi.org/10.1126/sciadv.adg1213.

Hersbach, H., and Coauthors, 2020: The ERA5 global reanalysis. *Quart. J. Roy. Meteor. Soc.*, **146**, 1999–2049, https://doi.org/10.1002/qj.3803.

Hoesly, R. M., and Coauthors, 2018: Historical (1750–2014) anthropogenic emissions of reactive gases and aerosols from the Community Emissions Data System (CEDS). *Geosci. Model Dev.*, **11**, 369–408, https://doi.org/10.5194/gmd-11-369-2018.

Hu, C., S. Yang, Q. Wu, Z. Li, J. Chen, K. Deng, T. Zhang, and C. Zhang, 2016: Shifting El Niño inhibits summer Arctic warming and Arctic sea-ice melting over the Canada Basin. *Nat. Commun.*, **7**, 11721, https://doi.org/10.1038/ncomms11721.

Hurrell, J. W., and Coauthors, 2013: The Community Earth System Model: A framework for collaborative research. *Bull. Amer. Meteor. Soc.*, **94**, 1339–1360, https://doi.org/10.1175/BAMS-D-12-00121.1.

Iizumi, T., J.-J. Luo, A. J. Challinor, G. Sakurai, M. Yokozawa, H. Sakuma, M. E. Brown, and T. Yamagata, 2014: Impacts of El Niño Southern Oscillation on the global yields of major crops. *Nat. Commun.*, **5**, 3712, https://doi.org/10.1038/ncomms4712.

Jiménez-Muñoz, J. C., C. Mattar, J. Barichivich, A. Santamaría-Artigas, K. Takahashi, Y. Malhi, J. A. Sobrino, and G. van der Schrier, 2016: Record-breaking warming and extreme drought in the Amazon rainforest during the course of El Niño 2015–2016. *Sci. Rep.*, **6**, 33130, https://doi.org/10.1038/srep33130.

Kang, S., Y. Zhang, Y. Qian, and H. Wang, 2020: A review of black carbon in snow and ice and its impact on the cryosphere. *Earth-Sci. Rev.*, **210**, 103346, https://doi.org/10.1016/j.earscirev.2020.103346.

Kim, M.-K., W. K. M. Lau, K.-M. Kim, J. Sang, Y.-H. Kim, and W.-S. Lee, 2016: Amplification of ENSO effects on Indian summer monsoon by absorbing aerosols. *Climate Dyn.*, **46**, 2657–2671, https://doi.org/10.1007/s00382-015-2722-y.

Kohyama, T., D. L. Hartmann, and D. S. Battisti, 2018: Weakening of nonlinear ENSO under global warming. *Geophys. Res. Lett.*, **45**, 8557–8567, https://doi.org/10.1029/2018GL079085.

Lack, D. A., and C. D. Cappa, 2010: Impact of brown and clear carbon on light absorption enhancement, single scatter albedo and absorption wavelength dependence of black carbon. *Atmos. Chem. Phys.*, **10**, 4207–4220, https://doi.org/10.5194/acp-10-4207-2010.

Latif, M., and N. S. Keenlyside, 2009: El Niño/Southern Oscillation response to global warming. *Proc. Natl. Acad. Sci. USA*, **106**, 20 578–20 583, https://doi.org/10.1073/pnas.0710860105.

Lee, H.-H., R. Z. Bar-Or, and C. Wang, 2017: Biomass burning aerosols and the low-visibility events in Southeast Asia. *Atmos. Chem. Phys.*, **17**, 965–980, https://doi.org/10.5194/acp-17-965-2017.

Lian, T., D. Chen, J. Ying, and Y. Tang, 2018: Tropical Pacific trends under global warming: El Niño-like or La Niña-like? *Natl. Sci. Rev.*, **5**, 810–812, https://doi.org/10.1093/nsr/nwy134.

Liu, X., and Coauthors, 2012: Toward a minimal representation of aerosols in climate models: Description and evaluation in the Community Atmosphere Model CAM5. *Geosci. Model Dev.*, **5**, 709–739, https://doi.org/10.5194/gmd-5-709-2012.

——, P.-L. Ma, H. Wang, S. Tilmes, B. Singh, R. C. Easter, S. J. Ghan, and P. J. Rasch, 2016: Description and evaluation of a new four-mode version of the modal aerosol module (MAM4) within version 5.3 of the Community Atmosphere Model. *Geosci. Model Dev.*, **9**, 505–522, https://doi.org/10.5194/gmd-9-505-2016.

Lou, S., Y. Yang, H. Wang, J. Lu, S. J. Smith, F. Liu, and P. J. Rasch, 2019a: Black carbon increases frequency of extreme ENSO events. *J. Climate*, **32**, 8323–8333, https://doi.org/10.1175/JCLI-D-19-0549.1.

——, ——, ——, S. J. Smith, Y. Qian, and P. J. Rasch, 2019b: Black carbon amplifies haze over the North China Plain by weakening the East Asian winter monsoon. *Geophys. Res. Lett.*, **46**, 452–460, https://doi.org/10.1029/2018GL080941.

Marlier, M. E., and Coauthors, 2015a: Regional air quality impacts of future fire emissions in Sumatra and Kalimantan. *Environ. Res. Lett.*, **10**, 054010, https://doi.org/10.1088/1748-9326/10/5/054010.

——, R. S. DeFries, P. S. Kim, S. N. Koplitz, D. J. Jacob, L. J. Mickley, and S. S. Myers, 2015b: Fire emissions and regional air quality impacts from fires in oil palm, timber, and logging concessions in Indonesia. *Environ. Res. Lett.*, **10**, 085005, https://doi.org/10.1088/1748-9326/10/8/085005.

Mcfarquhar, G. M., and H. Wang, 2006: Effects of aerosols on trade wind cumuli over the Indian Ocean: Model simulations. *Quart. J. Roy. Meteor. Soc.*, **132**, 821–843, https://doi.org/10.1256/qj.04.179.

Nicolas, J. P., and Coauthors, 2017: January 2016 extensive summer melt in West Antarctica favoured by strong El Niño. *Nat. Commun.*, **8**, 15799, https://doi.org/10.1038/ncomms15799.

Novakov, T., S. Menon, T. W. Kirchstetter, D. Koch, and J. E. Hansen, 2005: Aerosol organic carbon to black carbon ratios: Analysis of published data and implications for climate forcing. *J. Geophys. Res.*, **110**, D21205, https://doi.org/10.1029/2005JD005977.

Ramanathan, V., and G. Carmichael, 2008: Global and regional climate changes due to black carbon. *Nat. Geosci.*, **1**, 221–227, https://doi.org/10.1038/ngeo156.

Rashid, M., S. Yunus, R. Mat, S. Baharun, and P. Lestari, 2014: PM_{10} black carbon and ionic species concentration of urban atmosphere in Makassar of South Sulawesi Province, Indonesia. *Atmos. Pollut. Res.*, **5**, 610–615, https://doi.org/10.5094/APR.2014.070.

Sand, M., T. K. Berntsen, Ø. Seland, and J. E. Kristjánsson, 2013: Arctic surface temperature change to emissions of black carbon within Arctic or midlatitudes. *J. Geophys. Res. Atmos.*, **118**, 7788–7798, https://doi.org/10.1002/jgrd.50613.

——, T. Iversen, P. Bohlinger, A. Kirkevåg, I. Seierstad, Ø. Seland, and A. Sorteberg, 2015: A standardized global climate model study showing unique properties for the climate response to black carbon aerosols. *J. Climate*, **28**, 2512–2526, https://doi.org/10.1175/JCLI-D-14-00050.1.

Santoso, A., M. J. Mcphaden, and W. Cai, 2017: The defining characteristics of ENSO extremes and the strong 2015/2016 El Niño. *Rev. Geophys.*, **55**, 1079–1129, https://doi.org/10.1002/2017RG000560.

Sattar, Y., M. Rashid, M. Ramli, and B. Sabariah, 2014: Black carbon and elemental concentration of ambient particulate matter in Makassar Indonesia. *IOP Conf. Ser.*, **18**, 012099, https://doi.org/10.1088/1755-1315/18/1/012099.

Schwarz, J. P., and Coauthors, 2008: Measurement of the mixing state, mass, and optical size of individual black carbon particles in urban and biomass burning emissions. *Geophys. Res. Lett.*, **35**, L13810, https://doi.org/10.1029/2008GL033968.

Sobel, A. H., and E. D. Maloney, 2000: Effect of ENSO and the MJO on western North Pacific tropical cyclones. *Geophys. Res. Lett.*, **27**, 1739–1742, https://doi.org/10.1029/1999GL011043.

Stevenson, S. L., 2012: Significant changes to ENSO strength and impacts in the twenty-first century: Results from CMIP5. *Geophys. Res. Lett.*, **39**, L17703, https://doi.org/10.1029/2012GL052759.

Stjern, C. W., and Coauthors, 2017: Rapid adjustments cause weak surface temperature response to increased black carbon concentrations. *J. Geophys. Res. Atmos.*, **122**, 11 462–11 481, https://doi.org/10.1002/2017JD027326.

Stocker, T. F., and Coauthors, 2013: Frequently asked questions. *Climate Change 2013: The Physical Science Basis*,

T. F. Stocker et al., Eds., Cambridge University Press, 119–184, https://www.ipcc.ch/site/assets/uploads/2018/03/WG1AR5_SummaryVolume_FINAL.pdf.

Szopa, S., and Coauthors, 2021: Short-lived climate forcers. *Climate Change 2021: The Physical Science Basis*, V. Masson-Delmotte et al., Eds., Cambridge University Press, 817–922, https://doi.org/10.1017/9781009157896.008.

Thirumalai, K., P. N. DiNezio, Y. Okumura, and C. Deser, 2017: Extreme temperatures in Southeast Asia caused by El Niño and worsened by global warming. *Nat. Commun.*, **8**, 15531, https://doi.org/10.1038/ncomms15531.

Tosca, M. G., J. T. Randerson, C. S. Zender, M. G. Flanner, and P. J. Rasch, 2010: Do biomass burning aerosols intensify drought in equatorial Asia during El Niño? *Atmos. Chem. Phys.*, **10**, 3515–3528, https://doi.org/10.5194/acp-10-3515-2010.

Trentmann, J., and Coauthors, 2006: Modeling of biomass smoke injection into the lower stratosphere by a large forest fire (Part I): Reference simulation. *Atmos. Chem. Phys.*, **6**, 5247–5260, https://doi.org/10.5194/acp-6-5247-2006.

van Marle, M. J. E., and Coauthors, 2017: Historic global biomass burning emissions for CMIP6 (BB4CMIP) based on merging satellite observations with proxies and fire models (1750–2015). *Geosci. Model Dev.*, **10**, 3329–3357, https://doi.org/10.5194/gmd-10-3329-2017.

Wang, B., X. Luo, Y.-M. Yang, W. Sun, M. A. Cane, W. Cai, S.-W. Yeh, and J. Liu, 2019: Historical change of El Niño properties sheds light on future changes of extreme El Niño. *Proc. Natl. Acad. Sci. USA*, **116**, 22 512–22 517, https://doi.org/10.1073/pnas.1911130116.

Wang, C., 2007: Impact of direct radiative forcing of black carbon aerosols on tropical convective precipitation. *Geophys. Res. Lett.*, **34**, L05709, https://doi.org/10.1029/2006GL028416.

Wang, T., D. Guo, Y. Gao, H. Wang, F. Zheng, Y. Zhu, J. Miao, and Y. Hu, 2018: Modulation of ENSO evolution by strong tropical volcanic eruptions. *Climate Dyn.*, **51**, 2433–2453, https://doi.org/10.1007/s00382-017-4021-2.

Wang, Y., Y. Luo, J. Lu, and F. Liu, 2019: Changes in ENSO amplitude under climate warming and cooling. *Climate Dyn.*, **52**, 1871–1882, https://doi.org/10.1007/s00382-018-4224-1.

Ward, B., F. S. R. Pausata, and N. M. Maher, 2021: The sensitivity of the El Niño–Southern Oscillation to volcanic aerosol spatial distribution in the MPI grand ensemble. *Earth Syst. Dyn.*, **12**, 975–996, https://doi.org/10.5194/esd-12-975-2021.

Ward, P. J., M. Kummu, and U. Lall, 2016: Flood frequencies and durations and their response to El Niño Southern Oscillation: Global analysis. *J. Hydrol.*, **539**, 358–378, https://doi.org/10.1016/j.jhydrol.2016.05.045.

Wu, R., Z. Wen, and Z. He, 2013: ENSO contribution to aerosol variations over the Maritime Continent and the western North Pacific during 2000–10. *J. Climate*, **26**, 6541–6560, https://doi.org/10.1175/JCLI-D-12-00253.1.

Xie, S.-P., C. Deser, G. A. Vecchi, J. Ma, H. Teng, and A. T. Wittenberg, 2010: Global warming pattern formation: Sea surface temperature and rainfall. *J. Climate*, **23**, 966–986, https://doi.org/10.1175/2009JCLI3329.1.

Xu, L., and J.-Y. Yu, 2019: An ENSO-induced aerosol dipole in the west-central Pacific and its potential feedback to ENSO evolution. *Climate Dyn.*, **52**, 5115–5125, https://doi.org/10.1007/s00382-018-4435-5.

Yang, Y., and Coauthors, 2016a: Impacts of ENSO events on cloud radiative effects in preindustrial conditions: Changes in cloud fraction and their dependence on interactive aerosol emissions and concentrations. *J. Geophys. Res. Atmos.*, **121**, 6321–6335, https://doi.org/10.1002/2015JD024503.

——, L. M. Russell, S. Lou, M. A. Lamjiri, Y. Liu, B. Singh, and S. J. Ghan, 2016b: Changes in sea salt emissions enhance ENSO variability. *J. Climate*, **29**, 8575–8588, https://doi.org/10.1175/JCLI-D-16-0237.1.

——, H. Wang, S. J. Smith, P.-L. Ma, and P. J. Rasch, 2017: Source attribution of black carbon and its direct radiative forcing in China. *Atmos. Chem. Phys.*, **17**, 4319–4336, https://doi.org/10.5194/acp-17-4319-2017.

——, S. J. Smith, H. Wang, C. M. Mills, and P. J. Rasch, 2019: Variability, timescales, and nonlinearity in climate responses to black carbon emissions. *Atmos. Chem. Phys.*, **19**, 2405–2420, https://doi.org/10.5194/acp-19-2405-2019.

——, L. Zeng, H. Wang, P. Wang, and H. Liao, 2023: Climate effects of future aerosol reductions for achieving carbon neutrality in China. *Sci. Bull.*, **68**, 902–905, https://doi.org/10.1016/j.scib.2023.03.048.

Zhang, T., S. Yang, X. Jiang, and P. Zhao, 2016: Seasonal–interannual variation and prediction of wet and dry season rainfall over the Maritime Continent: Roles of ENSO and monsoon circulation. *J. Climate*, **29**, 3675–3695, https://doi.org/10.1175/JCLI-D-15-0222.1.